

Pattern Formation PDEs for Biological Applications

Neil Gabrielson, Kaan Volkan, and Naiwen Wang

July 5, 2025

Abstract

Chemical waves in the cell cortex are crucial for polarization, migration, and division. While several mathematical models based on reaction-diffusion systems have been developed to explain different wave behaviors, current models typically generate only traveling or standing waves, but not both. We computationally analyzed models by Mori et al. (2008) for standing waves and Michaud et al. (2022) for traveling waves. We discovered that the Michaud model can produce both standing and traveling wave behavior through parameter changes consistent with experimental observations, specifically by varying the F-actin diffusion coefficient from $D_F = 0.001$ (traveling) to $D_F = 0.4$ (standing). We also derived a simplified two-equation model based on the Michaud framework that generates both wave types through the same parameter mechanism. These findings suggest that cells may regulate wave patterns through biochemical control of diffusion rates.

Contents

1	Introduction	2
2	Existing Models	3
2.1	Gierer-Meinhardt Model for Reaction-Diffusion pattern formation	3
2.2	Mori Model for robust cell Polarization	5
2.3	Michaud Model for Cortical Excitability	6

3	Model Development	6
3.1	Mass Conservation Assumption	6
3.2	Simplification of Terms	7
3.3	Removal of Stochastic Noise	8
4	Numerical Methods	8
4.1	Finite Difference Method	8
4.2	Wave Analysis Pipeline	9
4.3	Optical Flow Pipeline	9
4.4	Wave Quantification Pipeline	11
5	Linear Stability and Bifurcation Analysis	12
5.1	Linear Stability Analysis	12
5.2	Bifurcation Analysis	15
5.3	Hughes Model	16
5.4	Numerical Continuation via BifurcationKit.jl	18
6	Results	21
6.1	Generation of Standing Waves in the Michaud Model	21
6.2	Wave Number in Michaud Model	26
6.3	Simplified Model Wave Behaviors	29
7	Discussion	30
7.1	Key Findings and Biological Significance	30
7.2	Future Directions	30

1 Introduction

Interactions between proteins in the cell cortex lead to the emergence of spatial patterns that are vital for cell functions such as motility, division, and embryonic development. Although the precise chemical mechanisms remain uncertain, several mathematical models have been proposed to explain these patterns.

We consider the following three existing models:

- **Gierer-Meinhardt:** A two-equation reaction-diffusion model that produces standing waves
- **Mori et al.:** A two-equation model designed to represent cell polarization that produces standing waves

- **Michaud et al.:** A three-equation model designed to represent cortical excitability that produces traveling waves

Existing models have been designed to either produce standing waves or traveling waves to mimic specific situations. However, experimental observations show that standing waves and traveling waves can occur in the same cells. In this project, we will pursue a unifying model guided by the following questions:

- Can a single model produce both traveling and standing waves through parameter changes that represent real biological processes?
- Can a two-equation model produce traveling waves? Can a three-equation model produce standing waves?

In pursuit of these findings, we utilized several computational methods, two of which were developed in-house. We utilized the Wave Analysis Pipeline, by Zac Swider, to measure the periodicity of generated waves to determine if a model produced standing or traveling waves through its second order autocorrelation data. We developed an optical flow analysis pipeline, utilizing OpenCV, to track wavefront and assess wave speed. We programmed a wave front quantification pipeline, based on established edge detection algorithms, to count the number of wavefront in a model.

We have identified standing waves produced by the Michaud model via changes to the diffusion rate of F-actin. We explore the transition between standing and traveling waves in the Michaud model through computational analysis.

We have also developed a simplified, two-equation system that maintains the general behavior of the Michaud model and produces both standing and traveling waves in a much smaller parameter space.

Furthermore, we performed various large parameter sweeps with in house analysis pipeline to identify the role of the parameters α and k_8 in the Michaud model and illustrated their relation to the number of waves generated in the cell surface.

2 Existing Models

2.1 Gierer-Meinhardt Model for Reaction-Diffusion pattern formation

While primarily known for his work in computer science, Alan Turing also made lasting contributions to the field of biology with his 1952 paper “A Chemical Basis For Morphogenesis.” Turing proposed that reaction-diffusion mechanisms could explain

the spontaneous emergence of spatial patterns from homogeneous initial conditions. Turing (1952) These “Turing patterns” have been used as a mathematical framework for a wide range of biological phenomena from animal spots to limb generation.

Reaction-diffusion models rely on interactions between two chemical species: a short-range **activator** that promotes its own production and a long-range **inhibitor** that suppresses the activator. When the inhibitor diffuses significantly faster than the activator, small random fluctuations can lead to stable spatial patterns through a process known as **diffusion-driven instability**.

The general framework for a reaction-diffusion system is given by the following system of partial differential equations:

$$\frac{\partial a}{\partial t} = f_1(a, h) + D\Delta a \quad (1)$$

$$\frac{\partial h}{\partial t} = f_2(a, h) + \delta\Delta h \quad (2)$$

where a represents the concentration of the activator, h represents the concentration of the inhibitor, f_1 and f_2 represent reaction functions between these chemicals, and D and δ represent diffusion coefficients, multiplied by the spatial Laplacian for each chemical, with $D \gg \delta$.

In 1972, the following reaction functions f_1 and f_2 were proposed for their ability to create stripes and spots: Gierer and Meinhardt (1972)

$$f_1(a, h) = c_1 - c_2a + \frac{a^2}{h(1 + Ka^2)} \quad (3)$$

$$f_2(a, h) = a^2 - h \quad (4)$$

This model successfully generates stable spatial patterns through diffusion-driven instability and has been widely applied to biological pattern formation. However, it only produces static patterns rather than the dynamic traveling waves that are also observed in cell cortices and lacks the specific protein interactions known to drive cortical excitability.

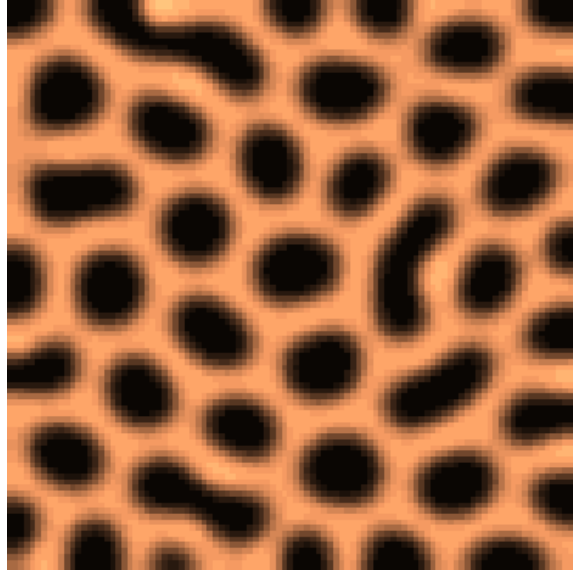


Figure 1: Spatial pattern resulting from computationally solving the Gierer-Meinhardt equations, where black represents high concentration of the active form a and orange represents low concentration of a .

2.2 Mori Model for robust cell Polarization

Cells have been observed to polarize robustly in response to transient stimuli. This behavior is essential to functions such as cell motility. The following system of equations has been proposed to model this behavior on a one-dimensional domain representing the cell diameter. Mori et al. (2008)

$$\frac{\partial u}{\partial t} = \left(b + \gamma \frac{u^n}{1+u^n} \right) v - Iu + D \frac{\partial^2 u}{\partial x^2} \quad (5)$$

$$\frac{\partial v}{\partial t} = -\left(b + \gamma \frac{u^n}{1+u^n} \right) v + Iu + \frac{\partial^2 v}{\partial x^2} \quad (6)$$

where u represents the active species and v represents the inactive species with diffusion coefficient $D \ll 1$.

This system effectively creates stable polarization patterns in response to stimuli and can exhibit some wave-like behavior. However, it is primarily designed for one-dimensional domains and is not intended to capture the traveling wave dynamics that experimentalists observe in cell cortices.

2.3 Michaud Model for Cortical Excitability

Certain cells have been observed to form dynamical patterns of traveling wave fronts in response to random, symmetry-breaking external stimuli. This phenomenon is known as **cortical excitability**, and its occurrence impacts the outcomes of developing embryos. The following three-species system was proposed to model cortical excitability based on experimental observations of frog and starfish oocytes. The proposed chemicals involved are active and inactive forms of proteins called Rho-GTPases as well as F-actin, which provides indirect negative feedback on active Rho through the reaction function $R(RT, RD, F)$. Michaud et al. (2022)

$$\frac{\partial RT}{\partial t} = R(RT, RD, F) + D_{RT}\nabla^2 RT \quad (7)$$

$$\frac{\partial RD}{\partial t} = k_5 - k_6 RD - R(RT, RD, F) + D_{RD}\nabla^2 RD \quad (8)$$

$$\frac{\partial F}{\partial t} = k_7 + k_8 \frac{RT^2}{1 + k_9 RT^2} - k_{10} dW F + D_F \nabla^2 F \quad (9)$$

with reaction function

$$R(RT, RD, F) = (k_0 + \alpha \frac{k_1 RT^3}{1 + k_2 RT^2}) RD - (k_3 + k_4(1 + \beta)F) RT \quad (10)$$

where RT represents active Rho-GTPase, RD represents inactive Rho-GTPase, F represents F-actin concentration, and dW represents a spatially correlated Gaussian noise field applied to F-actin degradation to model stochastic external processes and stimulate wave formation. The system exhibits excitable dynamics where small perturbations can trigger large-amplitude waves that propagate across the cortex.

These equations provide a good model for traveling wave behavior in the cell cortex; however, the original paper makes no reference to the production of standing waves by the model, and it relies on a stochastic noise term, dW , which makes it difficult to analyze.

3 Model Development

3.1 Mass Conservation Assumption

We simplified the Michaud model by imposing a mass-conservation constraint on the Rho-GTPase species, assuming that the total concentration of active and inactive GTPase is spatially and temporally constant:

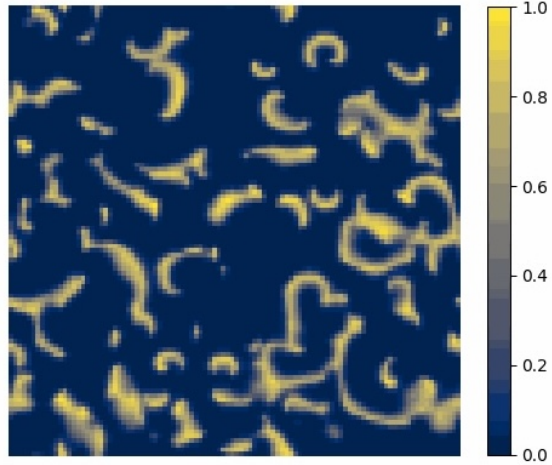


Figure 2: Snapshot of traveling waves produced by numerically solving the Michaud et al. model. The domain represents a small section of the cell cortex and the colormap represents the concentration of active Rho-GTPase (RT).

$$RT(x, t) + RD(x, t) = C \quad (11)$$

where C is a constant representing the total concentration of GTPase at every point. This assumption is biologically reasonable since Rho-GTPases cycle between active and inactive forms without net production or degradation on the timescales of wave dynamics. Substituting $RD = C - RT$ into the original system yields a two-equation model:

$$\frac{\partial RT}{\partial t} = (k_0 + \alpha \frac{k_1 RT^3}{1 + k_2 RT^2})(C - RT) - (k_3 + k_4(1 + \beta)F)RT + D_{RT}\Delta RT \quad (12)$$

$$\frac{\partial F}{\partial t} = k_7 + k_8 \frac{RT^2}{1 + k_9 RT^2} - k_{10}dWF + D_F\Delta F \quad (13)$$

3.2 Simplification of Terms

We further simplified each reaction term while preserving the essential biological relationships between chemical species:

$$\frac{\partial RT}{\partial t} = k_0 RT^2(1 - RT) - k_1 RTF + D_{RT}\Delta RT \quad (14)$$

$$\frac{\partial F}{\partial t} = k_2 RT - k_3 F + D_F\Delta F \quad (15)$$

The first term, $k_0 RT^2(1 - RT)$, captures autocatalytic activation of RT at low concentrations, with saturation when the concentration approaches 1. This polynomial form approximates the sigmoidal behavior of the Hill functions in the original model. The inhibition term, $-k_1 RTF$ represents depletion of RT based on local concentrations of both RT and F , consistent with the original model.

The F-actin equation gives production of F tied linearly to the concentration of RT , which closely approximates the Hill function behavior in the original model within our parameter range of interest. Depletion of F is linear with respect to local concentration, consistent with the original model.

3.3 Removal of Stochastic Noise

The Michaud model includes a stochastic noise term dW in the F-actin equation to initiate wave formation from homogeneous initial conditions. While this term is necessary for symmetry-breaking, it complicates the mathematical analysis of the system and creates unpredictable wave patterns.

We found that applying spatially correlated noise for the first 100 seconds, then removing it, is sufficient to generate stable, propagating wave patterns. This approach produces waves that propagate from fixed central points rather than appearing at random, making wave-speed analysis and mathematical analysis of the system simpler without ongoing stochastic interference.

4 Numerical Methods

4.1 Finite Difference Method

Finite Difference Method refers to the approximation of the derivative and the double derivative for computations on a finite discrete domain.

$$\frac{\partial u^2}{\partial^2 x} \approx \frac{u(x - h) - 2u(x) + u(x + h)}{h^2}$$

The extension of this method to two dimensions, namely the Laplacian, follows as

$$\Delta u = \frac{\partial u^2}{\partial^2 x} + \frac{\partial u^2}{\partial^2 y} \approx \frac{u(x-h, y) - 2u(x, y) + u(x+h, y)}{h^2} + \frac{u(x, y-h) - 2u(x, y) + u(x, y+h)}{h^2}$$

Assuming a matrix represents the 2D domain of the intended system, a minimal shift in the x, and y coordinates, namely " $\pm h$ ", matches with the notion of moving to the adjacent cell.

$$\begin{aligned}\Delta u &\approx \frac{u(x_{i-1}, y_i) - 2u(x_i, y_i) + u(x_{i+1}, y_i)}{h^2} + \frac{u(x_i, y_{i-1}) - 2u(x_i, y_i) + u(x_i, y_{i+1})}{h^2} \\ \Delta u &\approx \frac{u(x_{i-1}, y_i) + u(x_{i+1}, y_i) - 4u(x_i, y_i) + u(x_i, y_{i-1}) + u(x_i, y_{i+1})}{h^2}\end{aligned}$$

The following matrix shows an alternative way to write this equation.

$$\begin{bmatrix} 0 & 1 & 0 \\ 1 & -4 & 1 \\ 0 & 1 & 0 \end{bmatrix}$$

It serves as a future segue to mention that this matrix's convolution over a picture serves as an elementary edge detection algorithm as the second derivative of edges where the gradient is the highest yield larger values and inner-features with lower gradient are set to 0.

4.2 Wave Analysis Pipeline

The Wave analysis pipeline provides a method to measure the periodicity of waves in a given model. The model first simplifies the matrix through averaging groups of cells into one. Within the new matrix, cells values over time are tracked and recorded. Then, the second order autocorrelation of the time versus amplitude data yields the period of the signal.

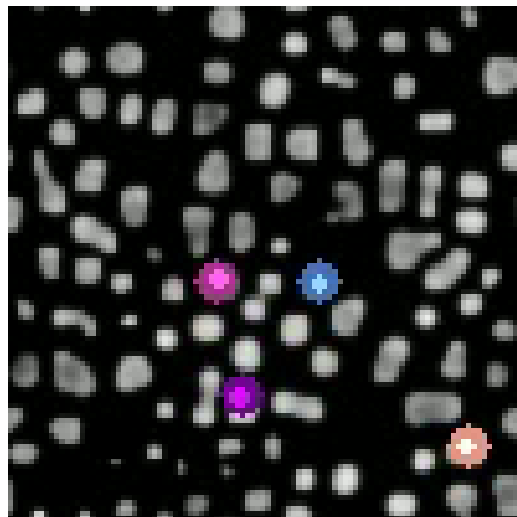
4.3 Optical Flow Pipeline

Optical flow pipeline utilizes an edge detection algorithm based on the Laplacian of the system to find the strongest 6 wave fronts, based on the magnitude of the Laplacian. It assigns the wavefront a marker, which stores its position, and every frame checks in its vicinity to find the new position and stores the positions in a list. The pixels traveled per frame yields the velocity. The nuance of the process stems from

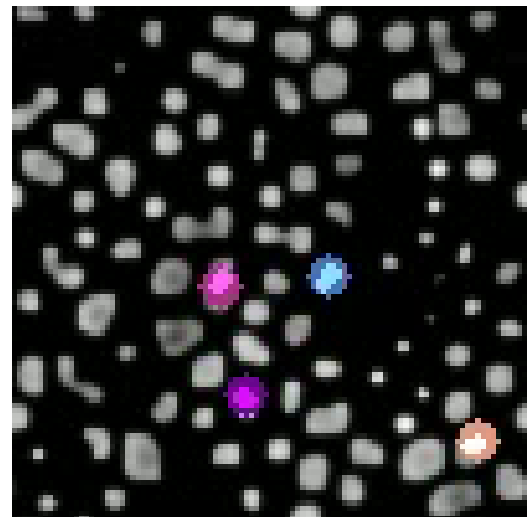
- Ensuring the markers are far apart to not track the same wavefront
- The small back and forth oscillations of a standing wave marker do not register as wave speed
- Ensuring that the markers track only one wave
- When a wave dissipates, the marker does not simply become a standing duck, pulling the average wave speed down significantly for the rest of its lifetime

As a result, the optical flow pipeline is optimized for various parameter ranges involving the density of waves, and also only pulls every 3rd or 4th position data to average out the small oscillatory observations on the standing waves. A final account of the initial and final position provide further clarity to the state of the waves.

The figure below shows the markers assigned to points on the Optical Flow Pipeline.

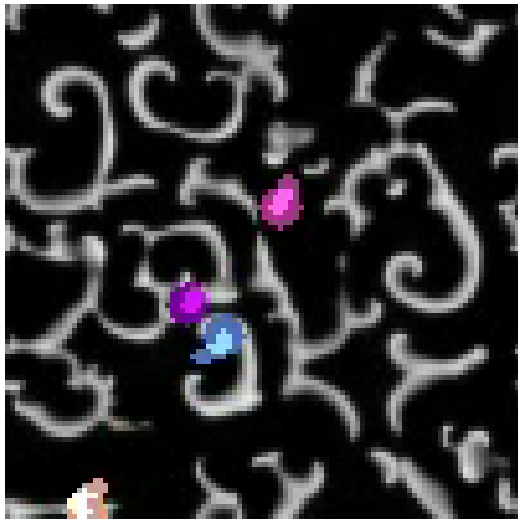


(a) Standing wave at $t = 60$

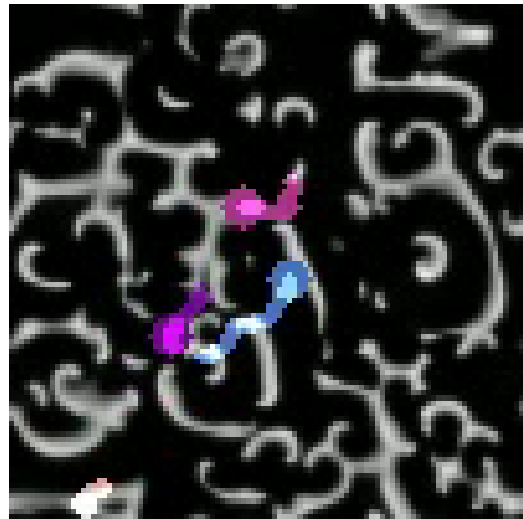


(b) Standing wave at $t = 360$

Figure 3: Optical Flow Pipeline on standing wave with Michaud Model at $D_F = 0.5$



(a) Standing wave at $t = 60$



(b) Standing wave at $t = 185$

Figure 4: Optical Flow Pipeline on traveling wave, Michaud Model at $D_F = 0.001$

4.4 Wave Quantification Pipeline

The Wave Quantification Pipeline first utilizes a gaussian blurring filter to remove noise from the simulation. Then, it applies the canny edge detection algorithm to isolate the wavefront. A separate algorithm then cuts down the thickness of the wavefront to single pixel thick to severe two waves which are different but touching each other. Finally, the smallest features are eliminated and the larger features are counted, yielding the number of waves.

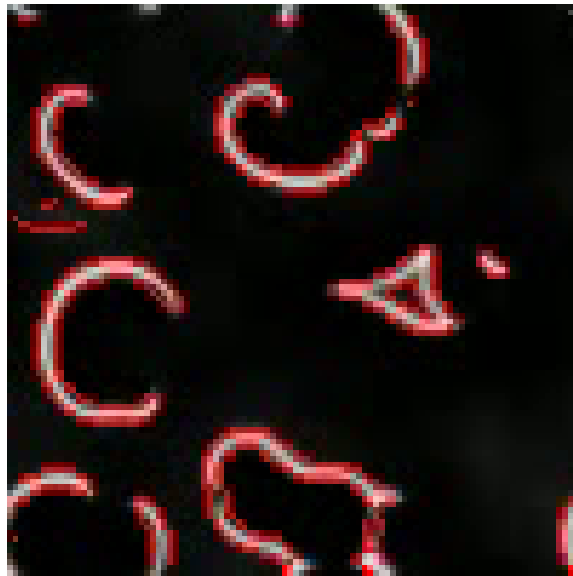


Figure 5: Post Processing view of wave fronts

5 Linear Stability and Bifurcation Analysis

In our project, we study pattern formation in systems of partial differential equations. In particular, we want to find traveling/standing waves (instability) that arise from small perturbations from a spatially uniform and time independent state in our biological system. Our primary sources on linear stability and bifurcation analysis are Logan (2015), Johnson (n.d.), van Voorn (n.d.). We will then try to replicate results from Hughes et al. (2024), a paper on a simplified F-actin and GTPase model inspired by Mori et al. (2008) and Holmes et al. (2012).

5.1 Linear Stability Analysis

For a partial differential equation, we define a corresponding **homogeneous steady-state solution** (HSS) u to be a function that satisfies the PDE and boundary conditions along with two properties:

- time independence (steady-state): $\frac{du}{dt} = 0$;
- and spatial uniformity (homogeneity): $\frac{du}{dx} = 0$;

where variables x and t denote space and time respectively.

Given a set of HSS to a differential equation, we want to understand whether solution is **linearly stable**. Informally, a sufficiently small perturbations to a linearly stable solution will die out. Formally, perform the following procedure to determine the stability of a HSS \bar{u} :

- First write a perturbation trial form (otherwise known as an Ansatz in German): $u(x, t) = \bar{u} + \varepsilon\phi(x, t)$ where \bar{u} is the HSS, $\varepsilon < 1$ and $\phi(x, t)$ is the perturbation function.
- We substitute this trial form into our original partial differential equation, discarding $\mathcal{O}(\varepsilon^2)$ terms (linearization) to obtain a linear PDE for the perturbation ϕ :

$$\frac{\partial \phi}{\partial t} = \mathcal{L}\phi$$

where \mathcal{L} is a linear operator.

- Finally, we verify spectral stability of the HSS \bar{u} . To do this, we assume a modal solution of the form $\phi(x, t) = e^{\sigma t}\psi(x)$ where $\sigma \in \mathbb{C}$ and $\psi(x)$ satisfies the same boundary conditions as ϕ . Substituting this expression into the linearized PDE yields an eigenvalue problem for the operator \mathcal{L} :

$$\sigma\psi(x) = \mathcal{L}\psi(x).$$

We will now determine the spectrum of \mathcal{L} denoted by $\sigma(\mathcal{L})$, which is defined as

$$\sigma(\mathcal{L}) = \{\lambda \in \mathbb{C} : \mathcal{L} - \lambda I \text{ is not invertible}\}.$$

Notice that in a finite dimensional space, this set is simply the set of eigenvalues of the matrix. While this can be done analytically, this project primarily uses numerical approximation of the eigenvalues: we discretize \mathcal{L} , assemble a converted matrix L , then we compute $\text{eig}(L)$. Furthermore, the eigenfunctions associated with each eigenvalue will be called spatial modes.

Obtaining the collection of eigenvalues σ_n of \mathcal{L} , we define the following cases:

- if $\text{Re}(\sigma_n) < 0$ for all n , then every spatial mode decays exponentially and \bar{u} is **linearly stable**.

- if $\operatorname{Re}(\sigma_n) > 0$ for some n , then the corresponding spatial mode grows and \bar{u} is **linearly unstable**.
- if for some eigenvalue $\operatorname{Re}(\sigma_{n_0}) = 0$ and no eigenvalue has positive real component, we obtain a candidate **bifurcation point**.

We will postpone the discussion of bifurcations until a later section.

Using an exercise solved from Logan (2015) to illustrate, consider the system of reaction diffusion equations on the spatial domain $0 < x < L$ given by

$$\begin{aligned} u_t &= \alpha u_{xx} + f(u, v) \\ v_t &= \beta v_{xx} + g(u, v) \end{aligned}$$

with no-flux boundary conditions $u_x = v_x = 0$ at $x = 0$ and $x = L$. Let \bar{u} and \bar{v} be steady-state solutions; functions that satisfy the PDE while being time independent (e.g. $\bar{u}_t = 0$). Note that a property of steady-state solutions is $f(\bar{u}, \bar{v}) = 0$.

We start by writing the perturbation equation. Let $u(x, t) = \bar{u} + U(x, t)$ and $v(x, t) = \bar{v} + V(x, t)$.

Then we Taylor expand about \bar{u} and \bar{v} and drop the higher order terms:

$$\begin{aligned} f(u, v) &= f(\bar{u} + U, \bar{v} + V) \\ &= f(\bar{u}, \bar{v}) + f_u(\bar{u}, \bar{v})U + f_v(\bar{u}, \bar{v})V + \dots \\ &= f_u(\bar{u}, \bar{v})U + f_v(\bar{u}, \bar{v})V + \dots \\ g(u, v) &= g(\bar{u} + U, \bar{v} + V) \\ &= g_u(\bar{u}, \bar{v})U + g_v(\bar{u}, \bar{v})V + \dots \end{aligned}$$

Now let $u_t = \alpha u_{xx} + f(u, v)$ and $v_t = \beta v_{xx} + g(u, v)$. Substitution into the original differential equation gives us

$$\begin{aligned} U_t &= \alpha U_{xx} + f_u(\bar{u}, \bar{v})U + f_v(\bar{u}, \bar{v})V, \\ V_t &= \beta V_{xx} + g_u(\bar{u}, \bar{v})U + g_v(\bar{u}, \bar{v})V. \end{aligned}$$

Now we rearrange the problem into matrix form. Let

$$\vec{W} = \begin{bmatrix} U(x, t) \\ V(x, t) \end{bmatrix}, D = \begin{bmatrix} \alpha & 0 \\ 0 & \beta \end{bmatrix} \quad (\alpha, \beta > 0), J = \begin{bmatrix} f_u(\bar{u}, \bar{v}) & f_v(\bar{u}, \bar{v}) \\ g_u(\bar{u}, \bar{v}) & g_v(\bar{u}, \bar{v}) \end{bmatrix}.$$

The differential equation is then $\vec{W}_t = D\vec{W}_{xx} + J\vec{W}$.

We will approach this problem by separation of variables: assume $\vec{W}(x, t) = \vec{C} = T(t)X(x)$ for constant vector \vec{C} . Substitution into the original PDE gives us the eigenvalue problem $T'(t) = \sigma T(t)$ for $\sigma = -\lambda$. Solving the Sturm-Liouville problem

$$X''(x) + \lambda X(x) = 0 \quad \text{for } X'(0) = X'(L) = 0,$$

we obtain a modal solution

$$\vec{W}_n(x, t) = \vec{C} e^{\sigma_n t} \cos\left(\frac{n\pi x}{L}\right) \quad (n = 0, 1, 2, \dots).$$

We will now set up the eigenvalue problem for the linear operator as referenced before. For notational simplicity, let $\phi_n(x) = \cos\left(\frac{n\pi x}{L}\right)$. By substituting our modal solution into the vector equation, we find that

$$\begin{aligned} \sigma_n \vec{C} e^{\sigma_n t} \phi_n &= D\left(-\frac{n^2\pi^2}{L^2}\vec{C} e^{\sigma_n t} \phi_n\right) + J\vec{C} e^{\sigma_n t} \phi_n \\ &\Rightarrow (\sigma_n I + \frac{n^2\pi^2}{L^2}D - J)\vec{C} = 0. \end{aligned}$$

Recall that $(\sigma_n I + \frac{n^2\pi^2}{L^2}D - J)\vec{C} = 0$ has a non-zero solution if and only if $\det(A) = 0$ for $A = (\sigma_n I + \frac{n^2\pi^2}{L^2}D - J)$. We will stop here before numerically solving for eigenvalues.

5.2 Bifurcation Analysis

To analyze the evolution of HSS given different parameters (constants) of a PDE or system of PDEs, we may plot the HSS values along a single parameter to produce 1 dimensional **bifurcation diagram**.

More precisely, given a system of differential equations (PDEs or ODEs),

$$\frac{du}{dt} = F(u, \lambda),$$

where $u \in \mathbb{R}^n$ is the state variable and $\lambda \in \mathbb{R}$ is the bifurcation parameter, the **bifurcation diagram** plots the solutions $\bar{u}(\lambda)$ which satisfy $F(u^*, \lambda) = 0$, the steady state solutions, as a function of λ .

Within a bifurcation diagram, a **bifurcation point** λ_c is where the qualitative set of solutions changes. At such a point, the following behavior may occur:

- the number of solutions may change,
- the solution's linear stability changes sign,

- or a new invariant set (not an HSS) appears (e.g. limit cycles).

A **branch** of the bifurcation diagram is defined as a connected smooth curve (or surface in multivariable cases) of solutions plotted against parameter λ ; note when the number of solutions change, the "splitting point" is singular, and indicates a new branch. Different branches correspond to different families of solutions.

We would like to now introduce some special bifurcation points that occur in a model discussed in a later section. Recall our definitions of linear stability and discussion of eigenvalues in the previous section.

A **Hopf Bifurcation** point λ_c occurs when a complex-conjugate pair of eigenvalues of the linearized system crosses the imaginary axis as λ crosses the critical λ_c . For $\lambda < \lambda_c$, the equilibrium is stable; for $\lambda > \lambda_c$, the equilibrium is unstable and a limit cycle (periodic orbit) is formed.

In PDEs or lattices, the linearized operator depends on a wave number k , the spatial frequency of a Fourier mode. Recall that the dispersion relation $\sigma(k, \lambda)$ gives the growth rate for each mode.

A **finite wave-number Hopf** bifurcation point, sometimes known as a wave/oscillatory Turing instability arises when critical eigenvalues cross the imaginary axis first at a non-zero wave number $k_c \neq 0$. This produces traveling or standing wave patterns with spatial period $2\pi/k_c$ that oscillate in time.

A **homogeneous Hopf** bifurcation point occurs when the zero wave number mode is critical. Every point in space oscillates in phase and no new structures appear onset.

We will also introduce a new instability. A **long-wave length instability** occurs when modes with small wave number grows. This instability results in phase separation instead of temporal oscillation when the system is perturbed.

5.3 Hughes Model

Recall the Mori "Wave-Pinning" model mentioned in an earlier section. This paper spawned many similar models, one of which is proposed by Hughes et al. (2024), which uses simply polynomial dependencies while maintaining conservation of mass. This polynomial model is given as

$$\begin{aligned}\frac{\partial u}{\partial t} &= (b + \gamma u)v - (1 + sF + u^2)u + D \frac{\partial^2 u}{\partial x^2}, \\ \frac{\partial v}{\partial t} &= -(b + \gamma u^2)v + (1 + sF + u^2)u + \frac{\partial^2 v}{\partial x^2}, \\ \frac{\partial F}{\partial t} &= \theta(p_0 + p_1 u - F) + D_F \frac{\partial^2 F}{\partial x^2}.\end{aligned}$$

We will also note that this polynomial model is "relatively" simpler to perform stability and bifurcation analysis compared to the Michaud and Mori models according to Hughes et al. (2024). We thus started here to understand linear stability and bifurcation analysis.

This system operates on a 1D domain and can be used with either periodic or Neumann boundary conditions, given respectively as

$$Q(0, t) = Q(L, t) \quad \text{and} \quad \partial_x Q(0, t) = \partial_x Q(L, t) = 0$$

where $Q(x, t) = (u, v, F)^T$. Furthermore, the system has mass conservation between the u, v , given as

$$M = \frac{1}{L} \int_0^L [u(x, t) + v(x, t)] dx$$

where M is a constant real number.

To find the homogeneous steady states of the system, we set each time and space derivative to zero, obtaining the system of equations

$$\begin{aligned} 0 &= (b + \gamma u^2)v - (1 - sF + u^2)u, \\ 0 &= \theta(p_0 + p_1 u - F), \\ 0 &= u + v - M. \end{aligned}$$

We note from Hughes et al. (2024) that the 3rd equation comes from mass conservation. Solving this system, we find that $v = M - u$, $F = p_0 + p_1 u$, and u is a root of the polynomial

$$\nu(u) = (b + \gamma u^2)(M - u) - (1 - s(p_0 + p_1 u) + u^2)u.$$

Most numerical continuation software start from an HSS and apply a variety of algorithms to calculate bifurcation points and branches of diagrams.

Parameter	Definition	Value
b	GTPase basal activation rate	[0,4.5]
γ	GTPase autocatalytic activation rate	3.557
s	Strength of F-actin negative feedback	[0,13]
θ	F-actin time scale parameter	0.6
p_0	F-actin basal assembly rate	0.8
p_1	GTPase-dependent F-actin assembly rate	3.8
D	Active GTPase rate of diffusion	0.1
D_F	F-actin rate of diffusion	0.001
M	Average total GTPase concentration	2,4.5

Figure 6: Table of constants from Hughes et al. (2024).

We would like to replicate the following bifurcation diagram plotting the HSS of F against the parameter s with $M = 2$ and $b = b_c \approx 0.067$ from Hughes et al. (2024).

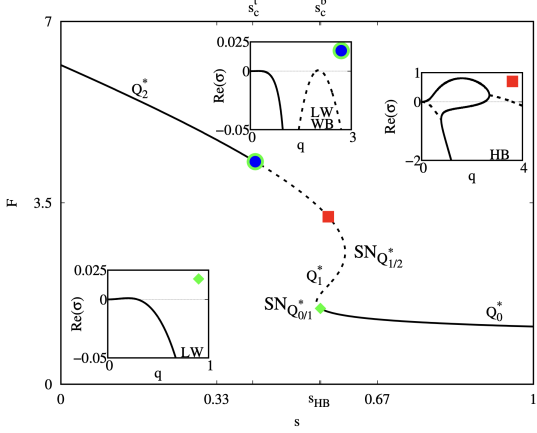


Figure 7: One-parameter bifurcation diagram plotting F against s from Hughes et al. (2024).

Note that from left to right, the blue point is a finite wave number Hopf, the red point is a LW instability onset, and the green point is a homogeneous Hopf bifurcation.

5.4 Numerical Continuation via BifurcationKit.jl

This project used the Julia programming language BifurcationKit package to numerically generate bifurcation diagrams and compute Hopf points. Unfortunately, the script for the numerical calculation of Hopf points and automatic bifurcation diagram for the Hughes model was incomplete by the end of the REU. The implementation encountered convergence errors from Newton iteration solvers, likely stemming from choice of HSS; note that choices for b and s are on a continuum, and changes the steady states.

In this section, we'll illustrate the capacity of the Julia package using a simpler reaction-diffusion system.

Let the Brusselator system in 1 dimension be defined as

$$\begin{aligned} \frac{\partial X}{\partial t} &= \frac{D_1}{l^2} \frac{\partial^2 X}{\partial z^2} + X^2 Y - (\beta + 1)X + \alpha \\ \frac{\partial Y}{\partial t} &= \frac{D_2}{l^2} \frac{\partial^2 Y}{\partial z^2} + \beta X - X^2 Y \end{aligned}$$

with Dirichlet boundary conditions

$$\begin{aligned} X(t, 0) &= X(t, 1) = \alpha \\ Y(t, 0) &= Y(t, 1) = \beta/\alpha. \end{aligned}$$

By setting the time and space derivatives, we find an HSS $X = \alpha, Y = \beta/\alpha$. Furthermore, let the initial conditions be $\alpha = 2, \beta = 5.45, D_1 = 0.008, D_2 = 0.004$.

Discretizing the PDE system and using BifurcationKit, we generate the following bifurcation diagram plotting X against the variable l .

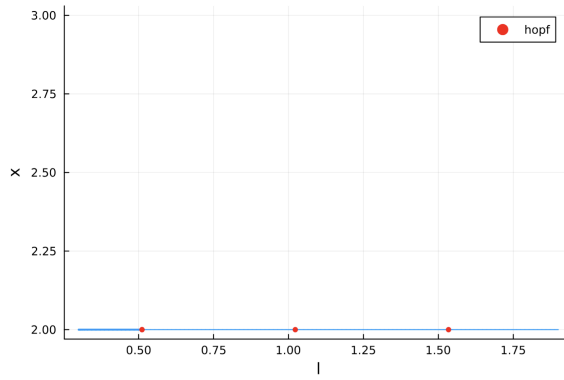


Figure 8: One-parameter bifurcation diagram plotting X against l .

The following figure outputs the location of Hopf points. For convenience, the software found Hopf points at approximately $l \approx 0.5, 1.0, 1.5$. From left to right, the points are Homogeneous Hopf, finite wave-number Hopf, and another higher order finite wave number Hopf. For $0.5 \leq l < 1.0$, we expect harmonic behavior with small deviations from equilibrium. From $1.0 \leq l < 1.5$, we expect single standing wave behavior. For $l > 1.5$, we expect two notes and a travelling wave pattern.

```

[Curve type: EquilibriumCont
└ Number of points: 120
└ Type of vectors: Vector{Float64}
└ Parameter l starts at 0.3, ends at 1.9
└ Algo: PNLG
└ Special points:
  - # 1,      hopf at l ≈ +0.51133101 ∈ (+0.51130339, +0.51133101), |δp|=3e-05, [converged], δ =
  - # 2,      hopf at l ≈ +1.02261272 ∈ (+1.02260927, +1.02261272), |δp|=3e-06, [converged], δ =
  - # 3,      hopf at l ≈ +1.53388402 ∈ (+1.53388396, +1.53388402), |δp|=5e-08, [converged], δ =
  - # 4, endpoint at l ≈ +1.90000000,

```

Figure 9: Calculated Hopf values.

The following figures are solutions to the Brusselator that exhibit the predicted behavior.

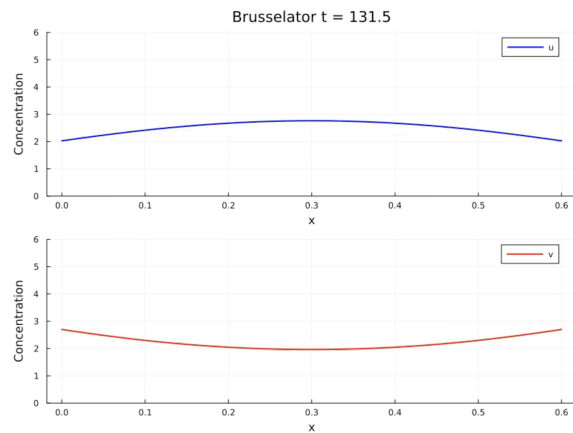


Figure 10: Brusseltor values for $l = 0.6$.

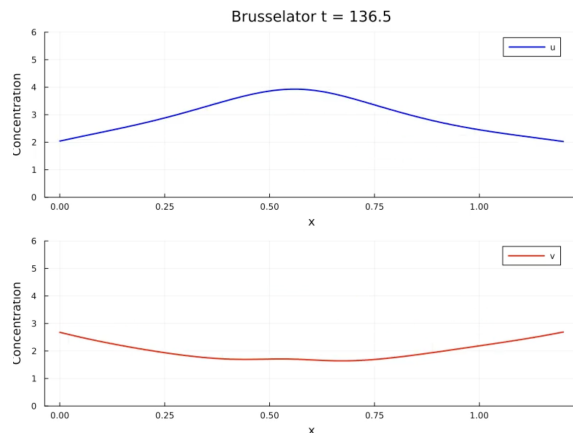


Figure 11: Brusseltor values for $l = 1.2$.

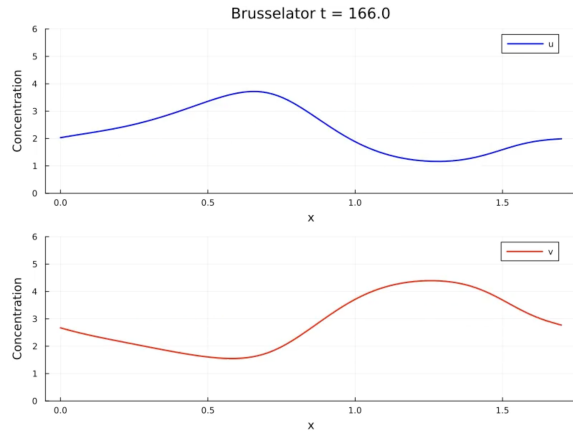


Figure 12: Brusselator values for $l = 1.7$.

6 Results

6.1 Generation of Standing Waves in the Michaud Model

The model proposed in Michaud et al. consists of 3 nonlinear partial differential equations. Within its studied parameter range, it generates traveling waves. Our targeted parameter sweep revealed stable solutions that yield stationary waves.

Furthermore, our work under-covered the existence of stable transitionary states, where stationary waves transition to traveling waves. These breakthroughs brings the Michaud et al. model a step closer to the biological observations where both traveling and stationary waves occur simultaneously.

Our parameter sweep reveals that the diffusion coefficient of F-actin, D_F , serves as the deciding factor to between traveling and standing waves.

The figure below displays 12 time stamps from Michaud et al. model with its default parameters. It produces traveling waves as advertised.

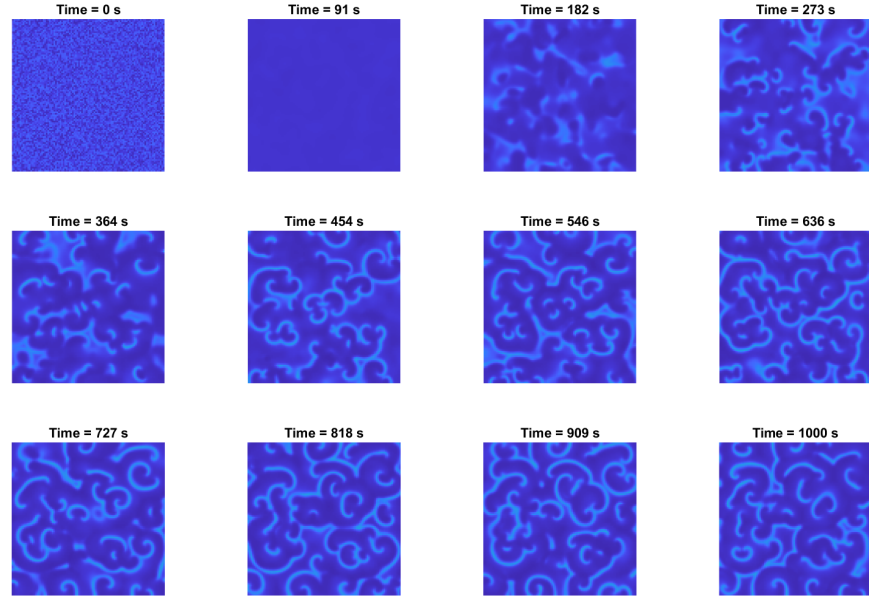


Figure 13: Snapshots of Michaud et al. model with default parameters, generating traveling waves

The figure below displays 12 time stamps from Michaud et al. model with default parameters with the exception of the diffusion coefficient of F-actin (D_F). It settles into discrete non-moving pockets of high and low RT concentration.

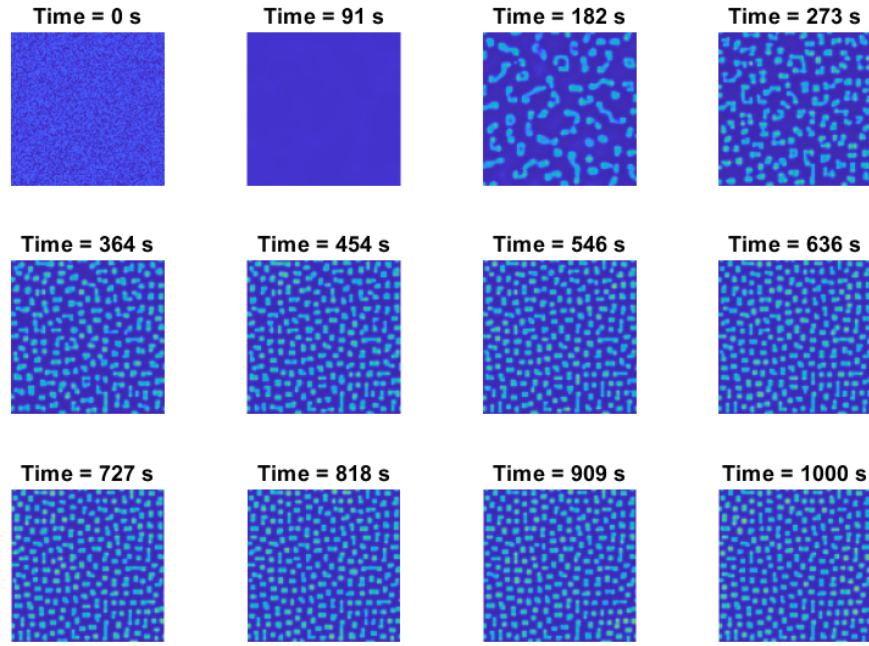


Figure 14: Michaud et al. model with $D_F = 0.6$

The transition state occurs where $0.05 < D_F < 0.3$. We utilized the optical flow pipeline to derive the median wave speed for various values of D_F . The figure below shows the variation of wave speed with respect to D_F .

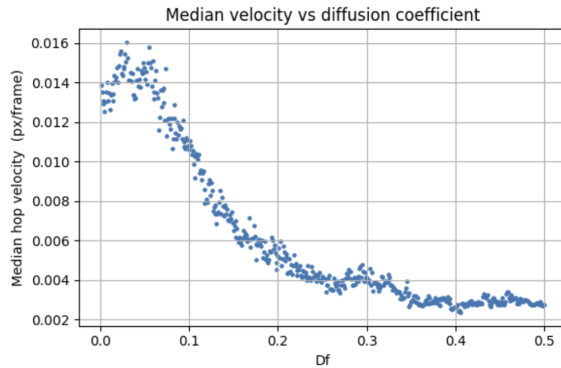


Figure 15: Mean velocity of waves in Michaud et al. model as a function of F-actin Diffusion Coefficient

This graph raises further questions about the relationship between the diffusion coefficient and wave speed. While the overall reduction of wave speed is evident as D_F reduces, an odd number of values take place where $0 < D_F < 0.04$, where the wave speed increases. A similar observation takes place where $0.25 < D_F < 0.3$ and $0.45 < D_F < 0.5$, but at a much smaller magnitude. For a more superficial look at the overall trend, the removal of the first 20 values shows strong coherence to an exponential decay of form $y = Ae^{-Bx} + C$

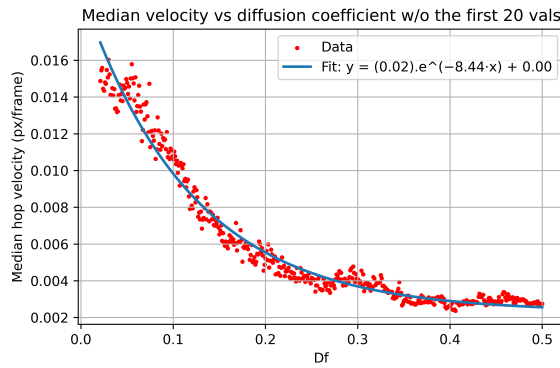


Figure 16: Wave speed as a function of D_F with the curve of best fit

The fit reveals parameters $A = 0.0175 \pm 0.0002$, $B = 8.4397 \pm 0.1738$, $C = 0.0023 \pm 0.0001$. The existence of the bumps suggest that a lower amplitude oscillation component to our current finding.

Another potential culprit for the unexpected behavior lies in the variability of the wave speed for the first 20 values. A high variability shows that further tuning

and adjustment of the model could yield values more in line with the expected. The figure below shows the median speed, the 75 percentile, and the 25th percentile of the measured wave speeds.

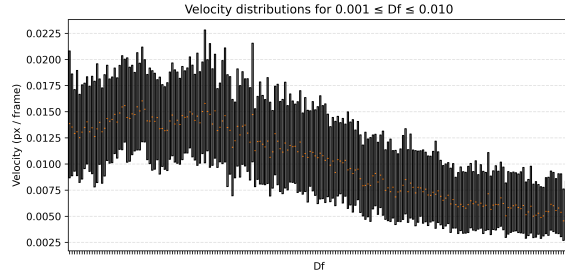


Figure 17: Median wave speed as a function of D_F with the 75th and 25th percentile included

The second order autocorrelation data presents an other method to confirm the wave behavior. We utilize the wave analysis pipeline to generate the following summary tables.

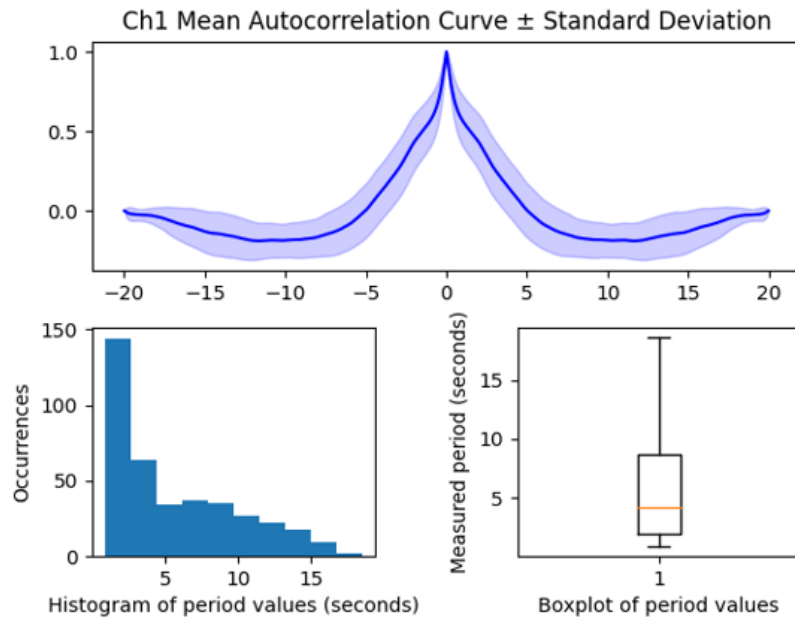


Figure 18: Summary data of standing wave with $D_F = 0.4$

The autocorrelation data shows the periodicity over time, and the central peak, representing the lack of it shows that the pockets of higher concentration settle into sections and stop changing with time. The width of the graph, presumably, comes from the developmental stage where the wave is still settling down.

The figure below shows the same data for the traveling wave with $D_F = 0.1$.

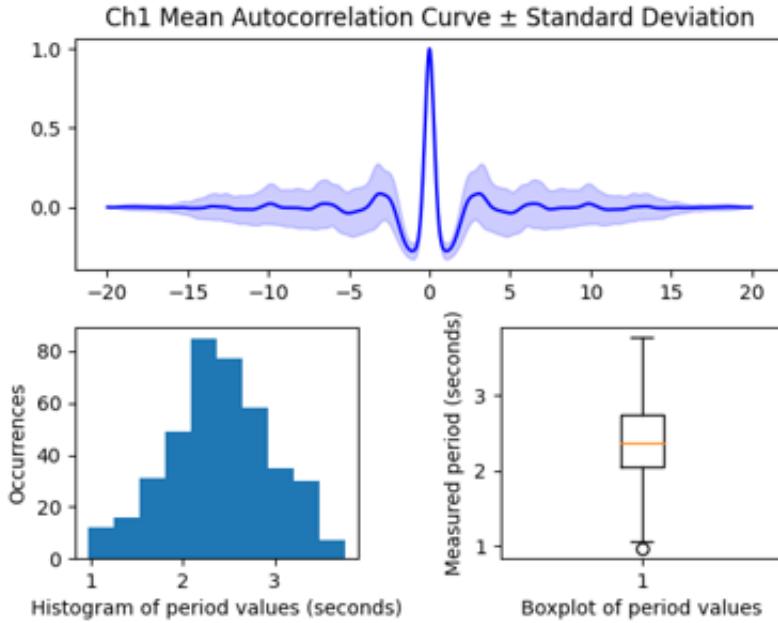


Figure 19: Summary data of standing wave with $D_F = 0.1$

A major significance of this result lays in the potential reproducibility of these results within a real world system, meaning the observed set of parameters are a subset of the physically possible and tunable parameters.

6.2 Wave Number in Michaud Model

As much as the formation of the waves, the number and density of the waves both matter. It had been proposed that the chemicals corresponding to k_8 and α in Michaud et al. model play a relevant role in controlling the number of the waves in the system.

We confirmed this through our in-house edge detection algorithm. The figure below shows how many waves were generated for the given values of α and k_8 .

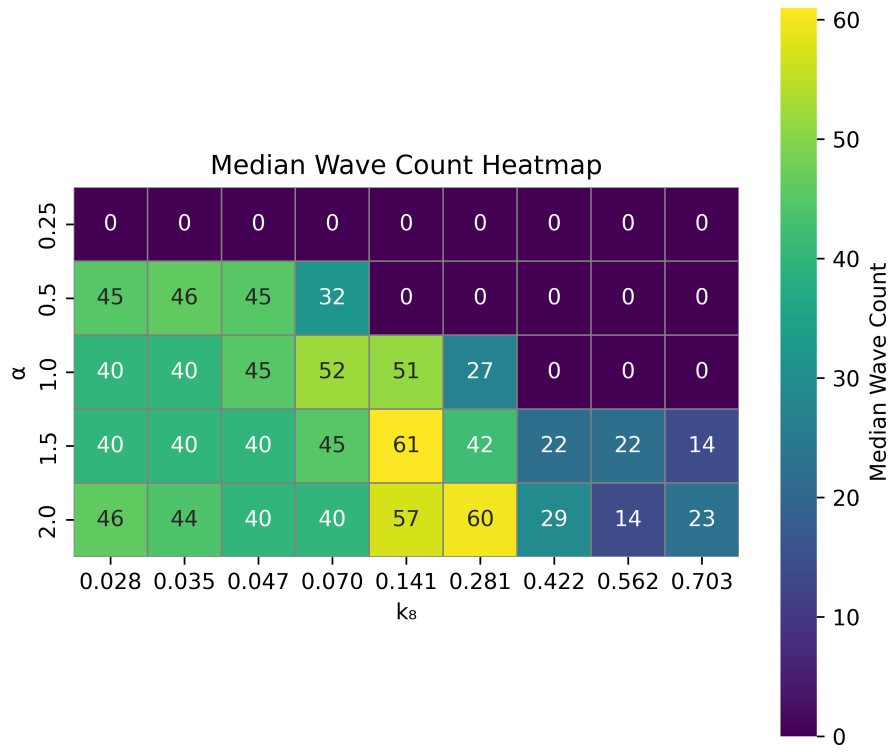


Figure 20: Median wave-count heatmap for range of α and k_8

The absence of waves, seen at the top edge, and the top left corner of the heatmap represents systems where wave formation failed. The figure below shows a snapshot of this at time= 500s for $\alpha = 0.25$ and $k_8 = 0.703$

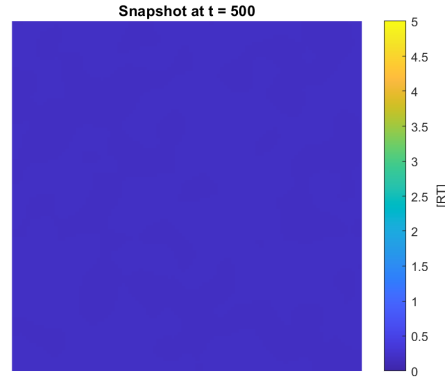
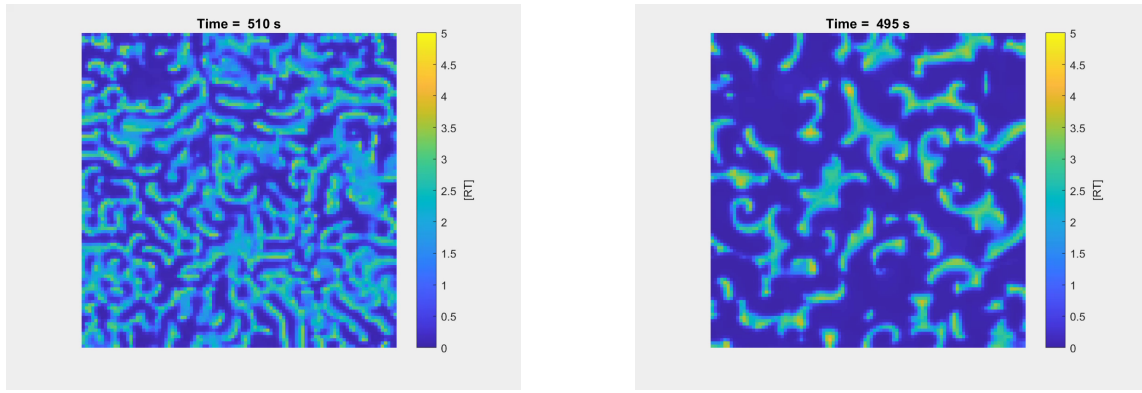


Figure 21: Snapshot of system at $t=500$ for $\alpha = 0.25$ and $k_8 = 0.703$

The figure below represents the system with the highest number of wavefront and system with the default parameters.



(a) Snapshot of system at $t=500$ for $\alpha = 1.5$ and $k_8 = 0.14$

(b) Snapshot of system at $t=500$ for $\alpha = 1.0$ and $k_8 = 0.14$

Figure 22: Snapshots of Michaud model with different parameters showcasing their effect on number of wavefront

These figures yield an intuitive confirmation to the data obtained from the wave number pipeline. Furthermore, as tunable parameters in the biological model, it opens an area of exploration.

6.3 Simplified Model Wave Behaviors

The simplified model introduced in Section 3 generates standing and traveling wave behavior similar to that of the Michaud model; however, the parameter space is significantly smaller, the terms are simpler, and the two-equation system enables more straightforward mathematical analysis.

A key advantage of the simplified model is the removal of the stochastic noise term, which allows us to generate traveling wave patterns that propagate from a steady central point rather than appearing randomly due to noise, making wave analysis more straightforward.

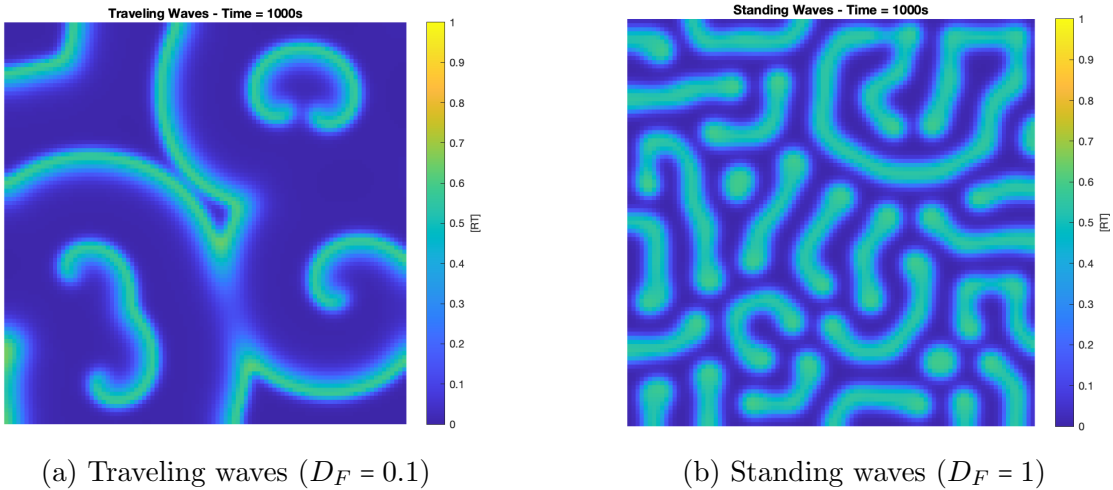


Figure 23: Snapshots of different wave behaviors from the simplified model, taken at time $t = 1000s$. (a) Traveling waves emerge with a low F-actin diffusion coefficient ($D_F = 0.1$). (b) Steady spatial patterns form when the F-actin diffusion coefficient is higher ($D_F = 1$). The colormap represents concentration of active Rho-GTPase (RT) over a 2-dimensional spatial domain.

The simplified model exhibits the same fundamental wave transition behavior as the Michaud model, with traveling waves occurring at low D_F values and standing waves emerging at higher D_F values.

This model maintains key biological mechanisms such as autocatalytic activation of Rho-GTPase and indirect inhibition by F-actin. Collaboration with experimentalists could validate the model’s application to real cortical systems.

Next steps include applying the analysis pipelines used on the Michaud model to our simplified model and conducting linear stability analysis on the system.

7 Discussion

7.1 Key Findings and Biological Significance

Our computational analysis revealed that the Michaud model can produce both standing and traveling waves through changes to the F-actin diffusion coefficient, D_F . The transition occurs where $0.05 < D_F < 0.3$, with traveling waves at low diffusion ($D_F = 0.001$) and standing waves at high diffusion ($D_F = 0.4$).

This finding suggests that cells could regulate wave patterns by controlling F-actin diffusion rates, providing a mechanism for switching between different cortical behaviors. The ability to produce both wave types within a single model aligns with experimental observations where cells exhibit both behaviors depending on context.

Our computational analysis also established a relation between the parameters α , k_8 and the wave number. Our findings show that variation from the default values of the model for k_8 and α tend to reduce the wave quantity, with the exception of increasing α by 50% while keeping k_8 the same, or increasing α by 100% with or without increasing k_8 by 50%.

7.2 Future Directions

Several promising directions emerge from this work:

- Experimental validation of F-actin diffusion thresholds in real cell systems
- Linear stability analysis of both the Michaud model and simplified model to understand the mathematical basis for wave transitions
- Application of the computational pipelines used on the Michaud model to the simplified model
- Collaboration with experimentalists to test model predictions about wave control mechanisms

Acknowledgments

We would like to thank Professor Calina Copos and our graduate advisor Tanishq Bhatia. We gratefully acknowledge funding from the Northeastern College of Science, the Northeastern Department of Mathematics, and the NSF RTG grant Algebraic Geometry and Representation Theory at Northeastern University DMS-1645877.

References

- A. Gierer and H. Meinhardt. A theory of biological pattern formation. *Kybernetik*, 12(1):30–39, 1972. doi: 10.1007/BF00289234.
- W. R. Holmes, A. E. Carlsson, and L. Edelstein-Keshet. Regimes of wave type patterning driven by refractory actin feedback: Transition from static polarization to dynamic wave behaviour. *Physical Biology*, 9(4):046005, 2012. doi: 10.1088/1478-3975/9/4/046005. URL <https://doi.org/10.1088/1478-3975/9/4/046005>.
- J. M. Hughes, C. Copos, Q. Vagne, and A. Mogilner. Travelling waves and wave pinning (polarity): Switching between random and directional cell motility, 2024. URL <https://arxiv.org/abs/2410.12213>.
- M. Johnson. Basic notes on stability and bifurcation, n.d. URL <https://matjohn.ku.edu/Notes/BasicStabilityNotes.pdf>. Accessed: 2025-06-25.
- J. D. Logan. *Applied Partial Differential Equations*. Undergraduate Texts in Mathematics. Springer Cham, 3 edition, 2015. ISBN 978-3-319-12493-3. doi: 10.1007/978-3-319-12493-3. URL <https://doi.org/10.1007/978-3-319-12493-3>. Springer Nature Switzerland AG 2015.
- A. Michaud, M. Leda, Z. T. Swider, S. Kim, J. He, J. Landino, J. R. Valley, J. Huisken, A. B. Goryachev, G. von Dassow, and W. M. Bement. A versatile cortical pattern-forming circuit based on Rho, F-actin, Ect2, and RGA-3/4. *Journal of Cell Biology*, 221(8):e202203017, August 2022. doi: 10.1083/jcb.202203017.
- Y. Mori, A. Jilkine, and L. Edelstein-Keshet. Wave-pinning and cell polarity from a bistable reaction-diffusion system. *Biophysical Journal*, 94(9):3684–3697, May 2008. doi: 10.1529/biophysj.107.120824.
- A. M. Turing. The chemical basis of morphogenesis. *Philosophical Transactions of the Royal Society of London. Series B, Biological Sciences*, 237(641):37–72, 1952. doi: 10.1098/rstb.1952.0012.
- G. van Voorn. Phd mini course: Introduction to bifurcation analysis. Companion material for the GLOBIF project, n.d. URL https://www.bio.vu.nl/thb/research/project/globif/Globif_text.pdf. Accessed: 2025-06-25.